Journal of Materials Chemistry A

Accepted Manuscript

ROYAL SOCIETY OF CHEMISTRY

www.rsc.org/materialsA

Journal of Materials Chemistry A

ARTICLE

Mesoporous Fe_2O_3 flakes of high aspect ratio encased within thin carbon skeleton for superior lithium-ion battery anodes†

Received 00th January 20xx,
Accepted 00th January 20xx

DOI: 10.1039/x0xx00000x

www.rsc.org/

Junhua Wang,[a] Mingxia Gao,*[a] Hongge Pan,[a] Yongfeng Liu,[a] Ze Zhang,[b] Jixue Li,[b] Qingmei Su,[c] Gaohui Du,[c] Min Zhu,[d] Liuzhang Ouyang,[d] Congxiao Shang [e] and Zhengxiao Guo [f]

Reticulated mesoporous Fe_2O_3@C flakes, consisting of nanocrystalline α-Fe_2O_3 encased within a thin carbon skeleton, are synthesized by using ferrocene as iron and carbon sources and a novel reaction agent of ammonium sulphate via a facile two-step heating route. Those flakes, of several nanometers thick and 1–2 μm in diameter, show high capacity, excellent cyclic stability and rate capability as an anode material for lithium-ion batteries (LIBs). An initial reversible capacity of 910 mAh g^{-1} at a discharge/charge current of 0.1 A g^{-1} is obtained, and the capacity shows a gradual increase during cycling, reaching a high capacity of 1080 mAh g^{-1} after 120 cycles. *In-situ* lithiation study by transmission electron microscopy reveals that the reticulated mesopores and the ultrathin feature of the Fe_2O_3@C flakes can largely accommodate mechanical stresses and volume expansion of Fe_2O_3 during lithiation, and hence maintain their integrity and provide excellent properties. The thin carbon skeleton not only facilitates the electronic conduction, but also inhibits the aggregation of the nanocrystalline Fe_2O_3 flakes. The facile fabrication method and the unique structure of the mesoporous Fe_2O_3@C flakes offer high performance for LIB anodes and great potential for other applications of Fe_2O_3.

Introduction

With the rapidly increasing demand for lithium-ion batteries (LIBs) of high-energy and high-power densities, extensive attention has been focused on high-performance anode materials, such as Si,[1-3] transition metal oxides,[4-8] new carbon materials[9] and SnO_2.[10, 11] Among these, Fe_2O_3 is one of the most promising candidates because of its high theoretical capacity (1007 mAh g^{-1}), nontoxicity, low cost and abundance.[12, 13] However, Fe_2O_3 anode materials suffer from large volume changes (>200 %)[12] and subsequently particle pulverization during lithium insertion and extraction, resulting in poor cycling stability. Reduction the particles to nano size can reduce the strain and hence alleviate the pulverization, and also provide facile lithiation kinetics due to the short diffusion path of lithium ions. However, nanoparticles are often coupled with large irreversible capacity loss associated with electrolyte degradation and suffer from severe agglomeration during cycling, thus damage their electrochemical property. Two-dimensional (2D) nanostructures offer an alternative architecture for high capacity, high-rate capability and cyclic stability. 2D structured electrode materials (nanosheets) possess large exposed surfaces and short lithium diffusion path. These are ideal frameworks for fast lithium storage.[14, 15] In addition, 2D structured iron oxides provide better resistance to the agglomeration of metallic Fe and thus the iron oxides during cycling than 0D nanoparticles, hence favouring the cycling stability. 2D structure also offers better fracture resistance than 1D structure, favouring the integrity of the active material during cycling.

The intrinsically low electrical conductivity of Fe_2O_3 is another drawback for it to become a high-performance anode material. In this regard, many researchers introduced conductive carbonaceous materials to form 2D structured Fe_2O_3-based materials, which are mostly layered Fe_2O_3/C composites, such as Fe_2O_3 platelets loaded onto graphene sheets,[16] layer-structured Fe_2O_3 nanodisk/reduced graphene oxide composites,[17] Fe_2O_3/CNTs combined microdisks.[18] The introduced carbonaceous materials can also buffer partially the volume changes of the iron oxide during cycling due to their flexible nature.

Porous and hollow structures are attractive in iron oxide anode materials.[19-23] The pores not only facilitate electrolyte storage and transportation, but also accommodate the

[a] State Key Laboratory of Silicon Materials, Key Laboratory of Advanced Materials and Applications for Batteries of Zhejiang Province & School of Materials Science and Engineering, Zhejiang University, Hangzhou, 310027, P.R. China. E-mail: gaomx@zju.edu.cn; Tel./Fax: +86-571-87952615
[b] Center of Electron Microscopy, State Key Laboratory of Silicon Materials & School of Materials Science and Engineering, Zhejiang University, Hangzhou, 310027, P.R. China
[c] Institute of Physical Chemistry, Zhejiang Normal University, Jinhua, 321004, P.R. China
[d] School of Materials Science and Engineering, Key Laboratory of Advanced Energy Storage Materials of Guangdong Province, South China University of Technology, Guangzhou 510640, P.R. China
[e] School of Environmental Sciences, University of East Anglia, NorwichNR4 7TJ, UK
[f] Department of Chemistry, University College London, London, WC1H 0AJ, UK.

† Electronic supplementary information (ESI) available: TG/DTA curves of the precursor, additional TEM images and EDX results of the precursor and Fe_2O_3@C flakes, qualitative test result of Fe^{2+} and Fe^{3+} in acidic 1,10-phenanthroline solution, TEM and SAED images of the flakes after 120 cycles. See DOI: 10.1039/x0xx00000x

volume change of electrode materials. The reported porous or hollow-structured iron oxide anode materials are mostly particle-shaped, such as spindle-like,[20] spherical[22] and hierarchical hollow spheres.[23] With further consideration of the advantages of 2D architectures and conductive carbonaceous materials, it is logical to synthesize novel architectured 2D carbon-coated porous iron oxides.

Ferrocene is a useful iron and carbon sources in the synthesis of carbon coated Fe_3O_4 (Fe_3O_4@C) composites with various architectures by solvothermal method,[24] catalytic pyrolysis[25] and solid state reaction,[26] etc. In the present study, novel architectured mesoporous 2D Fe_2O_3@C flakes (2D-FC) in which the Fe_2O_3 flakes are encased within a thin carbon skeleton were synthesized by using ferrocene as iron and carbon sources and a new reaction agent of ammonium sulphate (abbreviated as AS) via a facile two-step heating method. These porous Fe_2O_3@C flakes show a facet size of 1 – 2 μm and a thickness of *ca*. 10 nm. The carbon content is 5.5 wt. %. To the best of our knowledge, porous 2D-structured iron oxide with such a large aspect ratio had not been reported previously. The ultrathin thickness is supposed to facilitate the lithium diffusion and provide high resistance to the strain caused by the lithiation and de-lithiation, favouring the structural integrity of the flakes. The large facet size is hopefully to prevent the agglomeration of the reduced metallic Fe and hence Fe_2O_3 during cycles, and provides continuous electron transport pathways, hence favours the electron conduction of the electrode. These 2D-FC show superior electrochemical property as anode material for LIBs. The morphology and structural evolutions of the 2D-FC during the initial lithiation process are *in-situ* studied by transmission electron microscopy (TEM). Quantitative accommodation of the pores to the volume expansion of the Fe_2O_3 flakes during lithiation is experimentally reported. These ultrathin mesoporous 2D-FC show high strain-resistance and volume accommodation during lithiation, and hence maintains their integrity and offer excellent electrochemical property. The unique architecture of the porous 2D-FC provides new possibility in developing high-performance iron oxide-based anode materials for LIBs. Moreover, such a unique structure of mesoporous nano- Fe_2O_3@C flakes is believed helpful in other applications of Fe_2O_3 materials, such as magnetic materials, water treatment, field emitters and gas sensors,[27-29] etc.

Experimental section

Synthesis of mesoporous 2D Fe_2O_3@C flakes

Typically, 2 g ferrocene and 2 g AS (ammonium sulphate) were ground by mortar and pestle, and then loaded into a stainless steel autoclave of 50 mL in an argon-filled glove box (Labstar, M-Braun) and sealed. The sealed autoclave was put into a tube furnace and heat treated at 550 °C for 3 h to form a precursor. The resultant precursor was composed of 2D flakes. A subsequent calcination at 350 °C for 1 h in air was performed for the precursor. A heating rate of 5 °C min^{-1} was used. As a result, mesoporous 2D-FC were obtained. The 2D feature of the precursor was preserved after the calcination. To explore the growth process of the 2D flakes, different precursors were also prepared by heating the mixture of ferrocene and AS to different temperatures in the range of 300 – 550 °C without dwelling and dwelt at 550 °C for 1 h.

Material characterizations

The structures of the precursor and the 2D-FC were characterized by X-ray diffraction (XRD, X'Pert Pro, Cu Kα), Raman spectroscopy (Renishaw, inVia), scanning electron microscopy (SEM, Hitachi S4800), X-ray photoelectron spectroscopy (XPS, ESCALAB 250Xi, Thermo Scientific, Al Kα), transmission electron microscopy (TEM) , high resolution TEM (HRTEM, Philips-FEI Tecnai G2 F30), selected area electron diffraction (SAED) and energy dispersive X-ray (EDX). Thermogravimetric and differential thermal analyses (TG/DTA, TA SDT Q600) of the precursor was carried out in air from room temperature to 600 °C at a heating rate of 5 °C min^{-1}. The carbon contents of the precursor and the 2D-FC were measured by an element analyser (EA GmbH, Vario Micro). Specific surface area of the 2D-FC was measured by a Brunauer-Emmett-Teller (BET, NOVA 4000e, Quantachrome) method. Microstructural evolution of the precursor upon heating to different temperatures and dwelling for different periods was observed by SEM.

Electrochemical measurements

Electrochemical property of the 2D-FC was measured by using coin cells of CR2025 with Li foil as reference and counter electrode, and a polyethylene membrane (Celgard 2400) as separator. The working electrode was prepared by mixing the 2D-FC, Ketjen black, Super P and polyvinylidene fluoride (PVDF) in a weight ratio of 70: 10: 10: 10 to form a slurry, which was subsequently pasted onto a copper foil and dried at 120 °C for 14 h in vacuum. The 2D-FC loaded on each electrode was *ca*. 3 mg. The using of the combined 10 wt% Ketjen black and 10 wt% Super P as electronic conductive additives is intended to modify the electrochemical property of the anode. A solution of 1 M $LiPF_6$ in ethylene carbonate (EC)/dimethyl carbonate (DMC) (1: 1 by weight) was used as electrolyte. The cells were assembled in an argon-filled glove box with H_2O and O_2 contents less than 0.1 ppm (M-Braun). The cells were galvanostatically discharged and charged in a potential rang of 0 – 3 V vs. Li^+/Li at a current density of 0.1 A g^{-1} by using an electrochemical testing system (Neware Technology Co., China). High-rate capability of the 2D-FC was tested at discharge currents from 0.1 A g^{-1} to 2 A g^{-1} with a constant charge rate of 0.1 A g^{-1}. Cyclic voltammetry (CV) curve of the 2D-FC was measured on a multi-channel electrochemical testing system (MITS2.9-BT2000, Arbin) at a scan rate of 0.1 mV s^{-1} in a potential range of 0 – 3 V vs. Li^+/Li. All of the electrochemical tests were performed at 25±1 °C. The thickness change of the 2D-FC electrode after initial and 10 cycles of lithiation, and the morphology of the 2D-FC after 10 cycles of lithiation and de-lithiation at a current of 100 mA

g^{-1} are observed by SEM. The cell was disassembled in the glove box. Cross section of the electrode was used for the testing of the thickness change. For morphology observation of the 2D-FC after 10 cycles, the electrode material was scratched from the copper foil. The samples were all rinsed with dimethyl carbonate to remove the residual electrolyte prior to the SEM observation. For comparison, parallel experiments on selected electrochemical property and electrode thickness change during initial lithitaion of a commercial nano-particulate a-Fe_2O_3 (Hangzhou Wanjing New Material Co., China) with size of 30 – 120 nm were performed.

***In-situ* TEM study of lithiation**

In-situ study of the lithiation process of the porous 2D-FC was performed by TEM (JEOL, JEM-2100F). A half nano-cell consisting of a single porous Fe_2O_3@C flake as working electrode, a piece of Li_2O solid electrolyte and Li metal as the counter electrode was assembled inside the chamber of the microscope. The working electrode was prepared by naturally loading the flake on the tip of an Au rod (with a diameter of 0.25 mm). A tungsten rod was used to support the Li electrode prepared by scratching a piece of fresh lithium metal in an argon-filled glove box. The solid Li_2O electrolyte was prepared by shortly exposing a piece of fresh lithium metal in air. A negative bias of -1 V was applied to the nano-cell. The lithiation process was *in-situ* captured and recorded as a video, which was further edited as TEM images vs. the lithiation periods. The pore areas of the Fe_2O_3@C flake before and after the *in-situ* full lithiation were measured by image analysis on an optical microscope (VHX-100K, Japan). The structure of the fully lithiated flake was further analyzed by HRTEM and SAED.

Results and discussion

Fig. 1a shows the SEM morphology of the precursor obtained by heating the ferrocene and AS mixture in the sealed Ar-filled stainless steel reactor at 550 °C for 3 h. The precursor consists mainly of flakes with facet size of 1–2 μm and thickness of nanometer-order in addition to a few amounts of fragments. The flakes show smooth surface and almost solid feature under SEM observation; however, TEM observation shows that there are dense nanopores in size of 2 – 5 nm distributed evenly in the flakes. Fig. 1b and c shows the TEM/HRTEM images of the precursor under different magnifications. The bright contrast domains are the nanopores, as those circled in Fig. 1c. Distinguishable lattice fringes are hardly indentified by HRTEM and there is only diffused halo identified by SAED (the inset in Fig. 1c), indicating that the precursor is mostly amorphous.

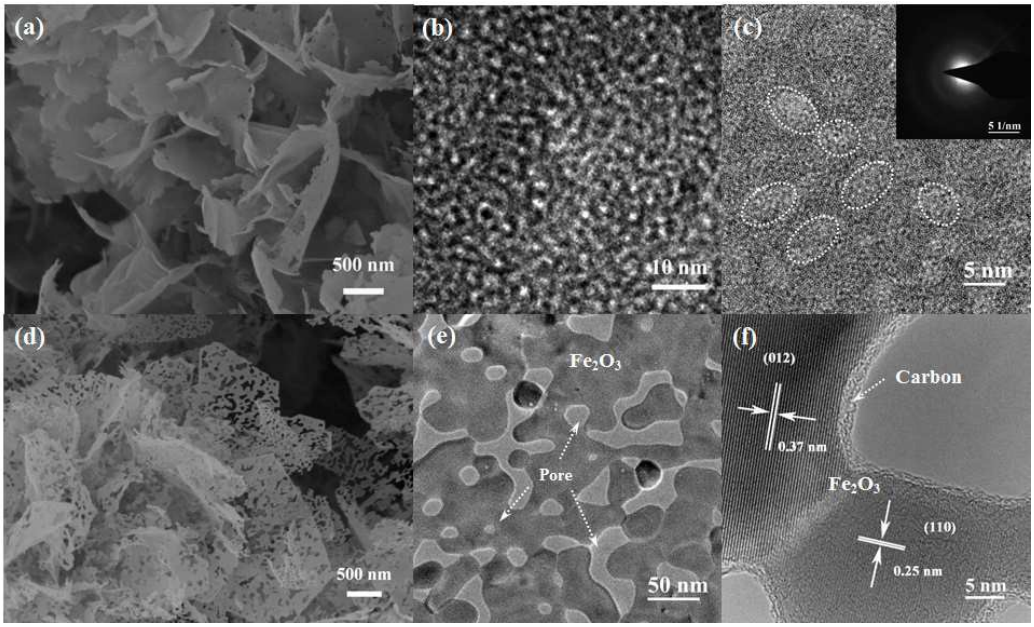

Fig. 1. (a) SEM morphology of the precursor obtained after heating the mixture of ferrocene and AS at 550 °C for 3 h in sealed Ar; (b) TEM and (c) HRTEM and SAED (the inset) images of the precursor; (d) SEM morphology of the calcined porous 2D-FC at 350 °C for 1 h in air; (e) TEM and (f) HRTEM images of the porous 2D-FC.

The decomposition of individual AS was extremely complex.[30,31] It was reported that AS was decomposed to gaseous products of H_2O, NH_3, SO_2 and N_2 in a rapid heating to 400 °C in an Ar carrying gas.[30] The decomposition temperature of ferrocene could be lowered to 350 °C with assisted reaction agents, such as isopropanol[24] and ammonium perchlorate,[26] though individual ferrocene is commonly not decomposed at temperature lower than 450 °C. The present heating temperature of 550 °C for the synthesis of the precursor is high. The bonded carbon in the ferrocene should be fully decomposed, especially with the impelling of the decomposition products of AS. The carbon content of the precursor detected by elemental analysis is 38.2 wt%, which is high. As inert Ar was used in the heating process, the

decomposed carbon was mostly maintained in the precursor. TG/DTA analysis of the precursor in air (Fig. S1†) shows that the weight loss and the heat release tend to be evident at 350 °C, indicating an evident gaseous reaction of the carbonaceous materials at this temperature. Therefore, calcination at 350 °C in air was adopted to reduce the carbon content and generate iron oxide.

Fig. 1d shows the SEM morphology of the calcined product of the precursor at 350 °C for 1 h. The 2D feature and the planar size of the precursor are preserved after the calcination. However, the size of the pores is evidently enlarged and the thickness of the flakes is greatly reduced. The aspect ratio of the planar size to the thickness is extremely high. In addition, the pores are fully penetrated through the flakes and some of them are interconnected, forming reticulated mesoporous structure. There is only 5.5 wt% C remained in the calcined product, which is significantly lower than that in the precursor. The carbon in the precursor was mostly oxidized to gaseous products of CO_2/CO during the calcination. Fig. 1e is a TEM image of the calcined flakes. The relatively light grey-contrasts are the pores, and the dark grey-contrast is iron oxide. Uneven size from several nanometers to several tens nanometers and irregular shape of the pores are clearly observed from Fig. 1e. Fig. 1f is a HRTEM image of the flakes, in which an extremely thin carbon coating in thickness of 1 – 2 nm is observed on the surface of the iron oxide. Grain boundary is visibly seen in the nano-crystalline pieces in Fig. 1f and the lattice fringes of 0.37 and 0.25 nm of the two grains are in good agreement with the (012) and (110) interplanar distances of α-Fe_2O_3, respectively. The Fe_2O_3 flakes are polycrystalline and are encased within a thin carbon skeleton. The formation of polycrystalline Fe_2O_3 flakes encased within a thin carbon skeleton is confirmed from other scopes, as shown in Fig. S2a and b†. The flexible carbon skeleton is helpful in supporting the mesoporous Fe_2O_3 flakes. It is further noted that most of the pores occur along the edges of the nanocrystalline Fe_2O_3 pieces, as shown in Fig. 1f and S2a†; however, there are also tiny micropores found occasionally inside individual crystalline Fe_2O_3 piece, as shown in Fig. S2b†.

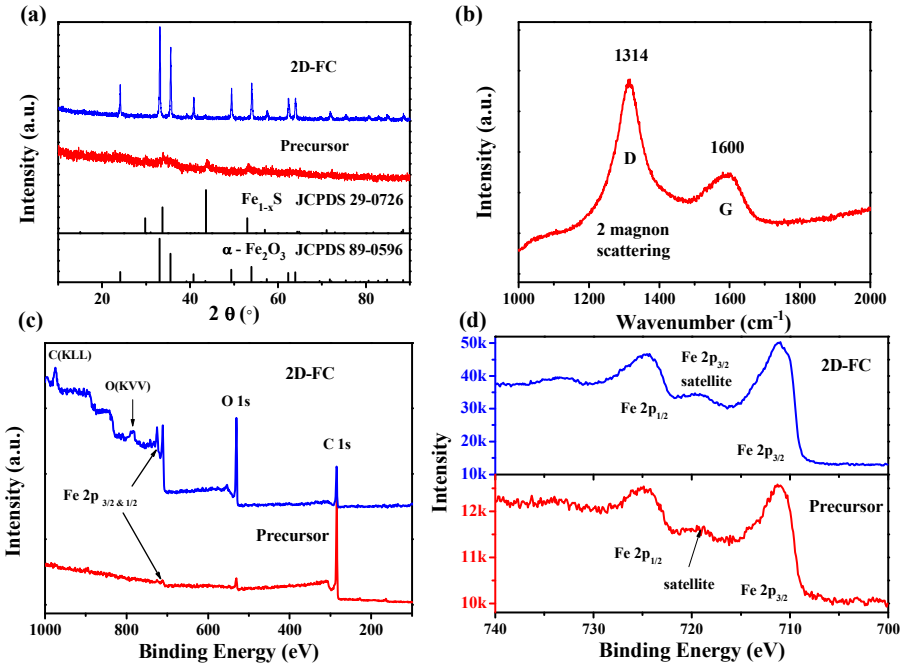

Fig. 2 (a) XRD patterns, (b) Raman spectrum, (c) XPS survey spectra and (d) the high resolution Fe 2p spectra of the precursor and 2D-FC.

Fig. 2a shows the XRD patterns of the precursor and the calcined 2D-FC. It is seen that there are only three weak peaks at 33.8º, 43.6º and 53.1º in the pattern of the precursor, which is indexed to $Fe_{1-x}S$ (JCPDS 29-0726), confirming the almost amorphous structure of the precursor. EDX analysis of the precursor under TEM (Fig. S3a†) shows that the precursor consists mainly of Fe, O, C and minuscule S. The signals of Cu and partial C are from the carbon coated copper grid supporter for the TEM analysis. That only minuscule amount of S was detected demonstrates that the S in AS was mostly decomposed, forming gaseous product. All the diffraction peaks of the 2D-FC are well indexed to α-Fe_2O_3 (JCPDS 89-0596), the result of which is well consistent with the HRTEM analysis (Fig. 1f). There is no any evidence of $Fe_{1-x}S$ detected in the 2D-FC, indicating that the $Fe_{1-x}S$ in the precursor was converted to α-Fe_2O_3 and S-containing gaseous product during the calcination process. EDX analysis of the 2D-FC (Fig. S3b†) also shows that there are only Fe, O and C detected, without S. Fig. 2b depicts the Raman spectrum of the 2D-FC. G-band of the graphitized carbon at 1600 cm^{-1} is visibly seen, while the D-band of carbon is partially overlapped by the

magnon scattering peak of α-Fe_2O_3 at 1314 cm^{-1}.[17] The result confirms the existence of amorphous carbon.

XPS survey spectra of the precursor and the 2D-FC are shown in Fig. 2c. The spectra were corrected using the measured C 1s peak with the standard C 1s peak. Peaks of Fe, O and C appear in both the precursor and the 2D-FC, whereas S is only detected in the precursor and the relative peak intensity is extremely low. The result is consistent with the EDX analysis that the precursor contains high content of C and minuscule amount of S. Moreover, the intensity of the Fe and O peaks in the precursor is extremely low and that of C is extremely high. As the atomic sensitivity factor of Fe is much higher than those of C and O, the weak intensity of Fe and O suggests that there is a thick carbon layer coated on the surface of the flakes of the precursor. The high peak intensity of Fe 2p and O 1s and the weak one of C 1s in the 2D-FC confirm that the thickness of the carbon coating on the surface of the Fe_2O_3 flakes was greatly reduced. The high resolution XPS spectra of Fe 2p of the precursor and 2D-FC are shown in Fig. 2d. It reveals that both Fe^{3+} and Fe^{2+} exist in the precursor. The calculated molar ratio of Fe^{3+}/Fe^{2+} of the precursor is *ca*. 2.08. Further considering the contribution of Fe^{2+} from $Fe_{1-x}S$ to the spectrum, it is likely that amorphous nonstoichiometric $Fe_{3-\delta}O_4$ formed in the precursor. Moreover, there is a weak satellite peak at *ca.* 719 eV in the spectrum of the precursor. Such peak is also reported in nonstoichiometric $Fe_{3-\delta}O_4$ films when the value of δ closes in upon the composition of γ-Fe_2O_3.[32]

For the 2D-FC, the fitting result is in good agreement with the main peaks of Fe $2p_{1/2}$ and Fe $2p_{3/2}$ of α-Fe_2O_3.[33] The two satellite peaks at *ca*. 719 and *ca*. 730 eV are associated to the Fe $2p_{3/2}$ and Fe $2p_{1/2}$ of α-Fe_2O_3, respectively.[33] The existence of both Fe^{2+} and Fe^{3+} in the precursor and there is only Fe^{3+} in the 2D-FC are further verified by a qualitative analytical method.[34] As shown in Fig. S4†, the dissolution of the precursor in 1,10-phenanthroline results in a red solution, indicating the existence of Fe^{2+} even there is a high concentration of Fe^{3+}, whereas that of the 2D-FC results in an achromatous solution, indicating the existence of only Fe^{3+}. The iron decomposed from ferrocene was oxidized by the O in the decomposed products of AS during the synthesis of the precursor. Meanwhile, the decomposed carbon acts as a reductive. As a result of a competition of the oxidation and reduction, an amorphous $Fe_{3-\delta}O_4$/C composite with a minuscule amount of $Fe_{1-x}S$ formed in the precursor. In the air calcination procedure, the nonstoichiometric $Fe_{3-\delta}O_4$ and $Fe_{1-x}S$ were fully converted into polycrystalline α-Fe_2O_3 under the strong oxidation environment and most of the carbon was oxidized, remaining only a low level.

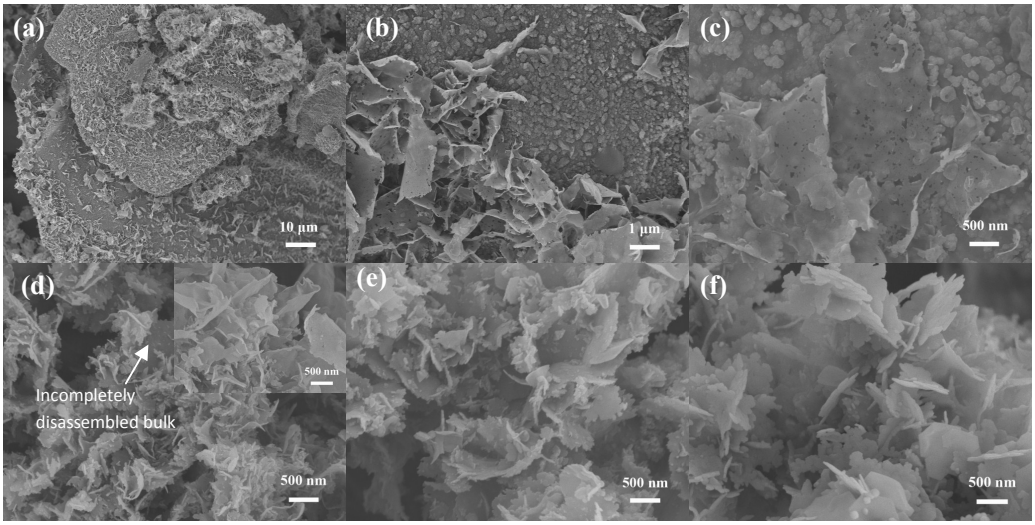

Fig. 3. SEM images of the precursors obtained by heating the mixture of ferrocene and AS to 350 °C without dwelling (a-c): (a) an overall image, (b)-(c) large magnification images from different micro-areas; to 450 °C without dwelling (d), the insert of (d) shows the grown flakes of the sample; to 550 °C without dwelling (e) and dwelling for 1 h (f).

The growth process of the 2D flakes of the precursor was evaluated by SEM observation of the microstructural evolution of the precursor during the heating and dwelling process. As the sample by heating to 300 °C was of high mucosity and not fully unreacted, moreover, the cover of the autoclave was tightly bonded by the reaction intermediate, this sample was not tested further. The precursor obtained by heating the mixture of ferrocene and AS to 350 °C shows an overall morphology of large bulk particles, as shown in Fig. 3a. A smaller magnification image showing the large distribution of the particle size is shown in Fig. 5Sa†. However, there are 2D-flakes growing on part of the surface of the large bulk particles. Fig. 3b is a large magnification image showing much clearly the 2D-falkes growing on the surface of the bulk particles. Moreover, there is still part of the surface of the large bulk particle without the growth of 2D flakes, instead, there is only fine particles generated. Fig. 3c is another type of typical SEM morphology observed in the precursor from other micro-area, which reveals that the 2D flakes of the precursor were initially exfoliated from the surface of the bulk particles. It is likely the fine particles on the surface of the bulk particles grow during the heating process with the further reaction of

the ferrocene and ammonium sulphate and connect to each other, forming an ultrathin film. Due to its mismatch to the bulk particles, the thin film exfoliated from the bulk particles, forming flakes. The growth process of the flakes is uneven. Dense flakes also formed on the surface of some bulk particles at this temperature, as shown in Fig. S5b†.

When the temperature is increased to 450 °C, as more flakes were exfoliated from the surface of the bulk particles, the large bulk particles almost disappear, which were mostly disassembled to 2D flakes as shown in Fig. 3d. A smaller magnification SEM image illustrating evidently the disassembling of the bulk particles is shown in Fig. S5c†. However, a few residual incompletely disassembled bulk pieces still exists as shown by the arrow in Fig. 3d. Moreover, the size of the flakes is not even. There are also micro-areas with size of flakes larger than those in Fig. 3d observed. The inset in Fig. 3d shows representatively those much grown flakes also formed at 450 °C. From an overall SEM observation, it is found that the area with small-sized flakes exists commonly with the appearance of residual incompletely disassembled bulks, and the area with large 2D flakes shows mostly flakes only. It is supposed that the latterly decomposed product forms both newly flakes and grows on the early formed small flakes. Fig. 3e and f shows the SEM images of the precursors by heating to 550 °C without dwelling and dwelt for 1 h, respectively. The residual bulks are further disassembled upon the heating to 550 °C, and the size of the flakes tends to be even. The small flakes formed at 450 °C grow further and the thickness of the flakes also increases. After dwelling for 1 h, the facet size and thickness of the flakes are more even and the morphology tends to be stable. The morphology is similar to that of the precursor dwelt for 3 h (Fig. 1a).

Fig. 4a shows the cycling performance and the Coulombic efficiency of the 2D-FC at a discharge/charge current of 0.1 A g^{-1}. For comparison, those of the commercial nano-particulate Fe_2O_3 anode are also shown. The 2D-FC show initial discharge and charge capacities of 1510 and 870 mAh g^{-1}, respectively. In comparison, the initial discharge/charge capacities of the commercial nano-Fe_2O_3 (1920/1110 mAh g^{-1}) are all higher than those of the 2D-FC. The specific surface area of the 2D-FC detected by the BET method is 24.5 m^2 g^{-1}, which is smaller than that of the commercial Fe_2O_3 nano-particles (34.5 m^2 g^{-1}). The structure difference is likely the main reason for the different initial capacities. The Coulombic efficiency of the 2D-FC increases rapidly from the initial one of 58% to 94% at the second cycle, and reaches a stable value of *ca*. 97% in the subsequent cycles. In comparison, the commercial one shows a lower Coulombic efficiency of 83% at the second cycle though the initial one is of a same value of 58%. Though its Coulombic efficiency also reaches the same stable value of *ca*. 97% after *ca*. 30 cycles, the capacity is rapidly declined, remaining only at 400 mAh g^{-1} after 20 cycles (Fig. 4a).

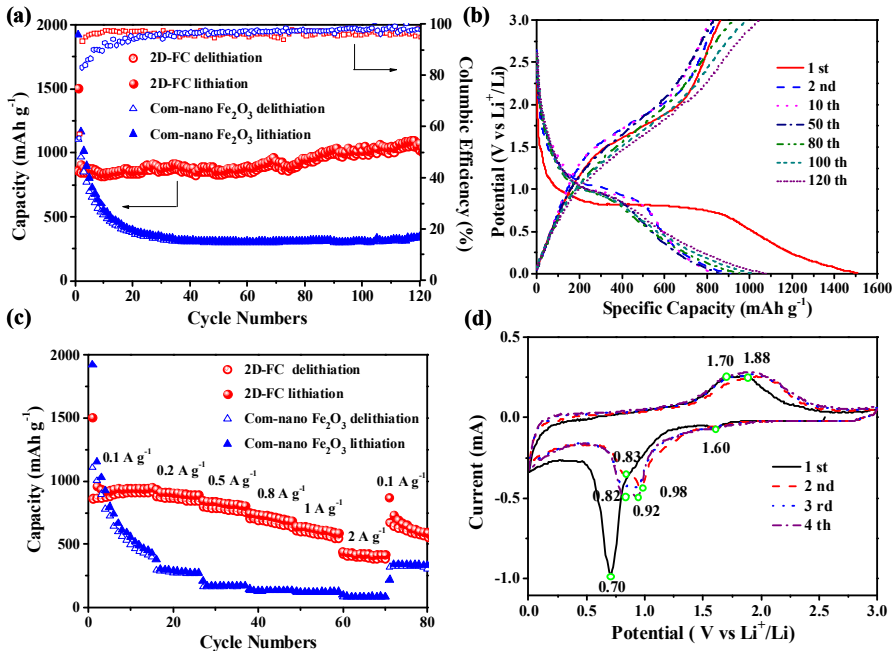

Fig.4 (a) Comparisons of cycling performance of the 2D-FC and commercial nano-particulate Fe_2O_3; (b) the voltage profiles of the 2D-FC for selected cycles; (c) the rate capability of the 2D-FC and commercial nano-particulate Fe_2O_3; (d) the CV curves of the 2D-FC of the initial four cycles.

The surface area of the Fe_2O_3 nanoparticles is higher than that of the 2D-FC and there are more sites for the diffusion of Li, however, it just shows a higher discharge/charge capacity at the first cycle. As the electronic conductivity of bare Fe_2O_3 is low and the nanoparticles suffer from severe agglomeration during cycling, the efficient use of the Fe_2O_3

nanoparticles is significantly reduced, thus damage greatly their electrochemical property. Such rapid capacity fading is common for bare Fe_2O_3 nanoparticles (without carbon coating), which are also reported in other literature.[35-37] Whereas the discharge capacity of 2D-FC is almost stable after the initial fading and tends to increase gradually in the following cycles, reaching a capacity of 1080 mAh g^{-1} after 120 cycles, which is increased by 170 mAh g^{-1} compared with the initial reversible one (910 mAh g^{-1}). The high cycling performance of the 2D-FC demonstrates that their structure is highly stable during cycling, which is attributed to the ultrathin thickness and porous structure of the 2D-FC, offering effective resistance to the strain during lithium insertion and extraction; the large facet size, which prevents the agglomeration of the flakes and the even carbon coating, which improves the electronic conductivity of the flakes. Increase in capacity after some initial cycles upon cycling is also reported in many other iron oxide systems[18, 38-42] and other transition oxide systems, such as CuO films,[43] which are proposed due to the activation and stabilization of the electrode materials,[18] the interfacial Li^+ storage in nanostructured materials,[38, 44] the reversible growth of the polymeric gel-like film by the kinetically activated electrolyte degradation[39-42], or/and the gradual decomposition of the irreversible Li_2O generated in the first discharge process.[43]

Voltage profiles of the porous 2D-FC for selected cycles are shown in Fig. 4b. It is worthy to note from the discharge profiles that the discharge plateaus in the comparatively high potential range of 0.8 – 1.1 V (vs. Li^+/Li) which associated with the conversion reaction of Fe^{3+} to Fe^0 are mostly overlapped from the 50th to 120th cycles, indicating that the discharge capacity from the conversion reaction of Fe^{3+} to Fe^0 is almost stable upon cycling. This means that the reason of the increasing capacity by the increasing reversibility of Li_2O generated at the initial lithitation as in the CuO anode[43] is not the main one for the present 2D-FC. As seen in Fig. 4b, the increase in discharge capacity upon cycling is mostly generated at the low potential range from the end of the flat plateau to the cut-off potential. Meanwhile, there is also increase in charge capacity upon cycling generated mostly at the relatively high potential range. Similar phenomena of the increase in discharge capacity at the low discharge potential and in charge capacity at the high charge potentials are also reported in other iron oxide systems, such as in the CNT@Fe_3O_4@C coaxial nanocables,[39] nano-Fe_3O_4/graphene composite,[40]carbon-coated Fe_2O_3 hollow nanohorns on CNT backbone,[42] Fe_2O_3/CNT film[45] and Fe_3O_4/pyrolytic graphite oxide composite,[46] etc. Though there are several reasons proposed for the increasing capacity in the literature as aforementioned, as the excess discharge capacity is delivered at the low potential range and the excess charge one is delivered at the high potential range, it is much likely that the reversible growth of a polymeric gel-like layer is a main one for the present 2D-FC, which is proposed due to a so-called "pseudo-capacitance" type behaviour.[47,48] Lou et al. [42] also propose that a reversible formation of an organic polymeric/gel-like layer by electrolyte decomposition at low potential is one of the possible reason for the increasing capacity upon cycling in a CNT@Fe_2O_3 system. Furthermore, the charge plateau corresponding to the oxidation of Fe^0 to Fe^{3+} tends to shift slightly to a low potential range upon cycling after the initial cycle, indicating a much facile lithium extraction with cycling.

High-rate performances of the porous 2D-FC and the commercial nano-particulate Fe_2O_3 at discharge currents up to 2 A g^{-1} are shown in Fig. 4c. Capacities of 780, 710, 610 and 420 mAh g^{-1} are achieved at 0.5, 0.8, 1 and 2 A g^{-1}, respectively, for the 2D-FC anode. Whereas the capacity is only 300 and 100 mAh g^{-1} at discharge currents of 0.2 and 2 A g^{-1}, respectively, for the commercial nano-particulate Fe_2O_3. The capacity of the 2D-FC is recovered to 900 mAh g^{-1} when the discharge current returns to 0.1 A g^{-1} after the testing of 2 A g^{-1}. The initially recovered capacity is only slightly lower than the initial reversible capacity. However, it seems that the cycling stability is somewhat reduced after the high-rate cycling.

Though the present 2D-FC has low carbon content (5.5 wt%) and low specific surface area (24.5 m^2 g^{-1}), its reversible specific capacity and cycling stability are superior than other reported 2D Fe_2O_3/C composites, such as the one of platelet Fe_2O_3 loaded on graphene sheet with a relatively high carbon content of 59 wt% and a large specific surface area of 174 m^2 g^{-1},[16] Fe_2O_3/CNTs microdiskes with a thickness of *ca*. 150 nm and a diameter of *ca*. 1.1 μm (carbon content was not reported).[18] The reversible specific capacity and cycling stability of the present 2D-FC are also comparable with the 2D nanosheets of *a*-Fe_2O_3 nanoplatelets sandwiched between graphene layers which with a high graphene content of 47 wt%.[27] The unique structure of the mesoporous and ultrathin feature, the high aspect ratio and the even carbon coating of the present 2D-FC play synergetic roles in improving the electrochemical performance.

CV curves of the porous 2D-FC of the initial four cycles acquired at a scanning rate of 0.1 mV s^{-1} are shown in Fig. 4d. There is a large cathodic peak centered at *ca.* 0.7 V in the initial sweep, corresponding to the common conversion reaction of Fe_2O_3 with lithium ions to form Fe and Li_2O, the SEI formation and the electrolyte decomposition, though the exact values are slightly different from different groups.[49,50] The weak cathodic peak centered at *ca*. 1.6 V in the initial sweep is attributed to the lithium insertion to Fe_2O_3, forming $Li_xFe_2O_3$, as reported previously.[51] These peaks disappear in the following cycles, indicating their irreversible feature. In the initial anodic process, two anodic peaks appear at 1.70 and 1.88 V. Two anodic peaks are also reported in other Fe_2O_3/C systems, which are attributed to the oxidation of Fe^0 to Fe^{2+} and Fe^{3+}.[51, 52] However, one anodic peak feature is also found in the CV curve of Fe_2O_3/C composites.[35,53] The difference existing in the redox peaks in the CV curves is supposed due to the different microstructures of the Fe_2O_3/C composites. In the subsequent cycles, the cathode peaks shift to a higher potential range due to the structural modification and the strain induced in the iron oxide after the first cycle. The splitting of the cathodic peak to two peaks in the

subsequent cycles indicates a two-step reduction of iron oxide. Moreover, the intensity of the two cathodic peaks increases with the cycling from the 2nd to 4th cycle, especially for the one at the comparatively lower potential, indicating a capacity increasing, though the peak potential shifts to slightly lower values from 0.83/0.98 to 0.82/0.92 V (vs. Li^+/Li), showing a slight polarization. The anodic peaks slightly shift to high potentials after the first cycle. However, the reversibility is high after the second cycle.

Fig. 5a shows schematically the nano-half cell and the lithiation setup of the *in-situ* TEM study of lithiation of the mesoporous 2D-FC. Fig. 5b is the TEM image of the pristine flake before lithiation. Fig. 5c – f show the morphological and structural evolution of the flake as a function of lithiation period, which was performed from the bottom to the top of the images as marked by the blue dot arrows. The white dash line marks the lithiation front. Fig. 5g is the image of the fully lithiated state. It is seen that the pores shrink and the Fe_2O_3 expand upon lithiation. The dark contrast areas generated at the lithiation front as marked by the red arrows are the mechanical strain deformation. As seen in Fig. 5c, there is less strain deformation at the beginning of the lithiation, as only a few amounts of lithium ions were inserted. With the further lithiation, the strain deformation became large, as seen in Fig. 5d and e. However, the mechanical stress releases readily during the lithiation process. It is worthy to note that there is no crack generated after the full lithiation, as seen in Fig. 5f. The ultrathin and porous feature of the flake contributes greatly the integrity.

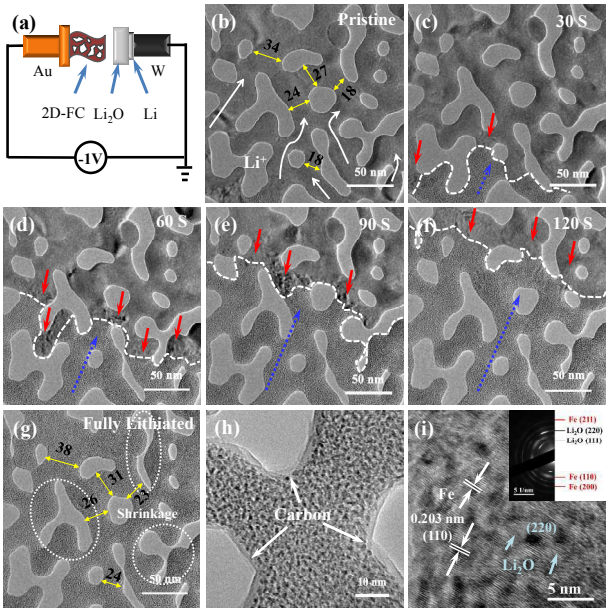

Fig. 5 *In-situ* TEM study of the porous 2D-FC during initial lithiation: (a) schematic illustration of the half nano-cell and the lithiation setup; (b) TEM image of the pristine porous 2D-FC; (c – f) morphological and structural evolutions of the porous flake as a function of lithiation period. (g) TEM image of the fully lithiated flake; (h) large magnification TEM image of the fully lithiated flake; (i) HRTEM image of the fully lithiated flake. The inset in (i) is the SAED pattern of the fully lithiated flake.

The pore area of the flake detected by image analysis shows a decrease from 35.5 % for the pristine state to 27.9 % after the fully lithiated state. The linear expansion of the Fe_2O_3 flake measured semiquantitatively from the selected areas marked in Fig. 5b and g is in the range of 8 – 28 %. The different expansions of the detected areas are likely due to their different spatial factors, such as their spatial position, the size and distribution of the pores around, etc. In comparison, a nano-Fe_2O_3 particle of a Fe_2O_3/graphene composite was reported with a linear expansion of *ca*. 20 % after lithiation, in which the particle was expanded from 47.6 to 57.2 nm.[54] The present mesopores provide sufficient space for accommodating the volume expansion of the Fe_2O_3 flake. Considerable residual pores maintain after full lithiation, as shown in Fig. 5g. Compared with the common theoretical volume expansion of 200 % for the full lithiation of Fe_2O_3,[12] it is likely that the present 2D-FC exhibits much less volume change. Fig. 5h is a large magnification TEM image of the fully lithiated flake, which shows that the carbon skeleton is well preserved and tightly coated on the surface of the flake. HRTEM analysis of the fully lithiated flake, Fig. 5i, further shows that there are ultra-fine nano Fe and Li_2O clusters formed. The SAED pattern shown as the inset of Fig. 5i confirms the formation of crystalline Fe and Li_2O.

The thickness change of the 2D-FC electrode after initial and 10 cycles of lithiation is further tested and shown in Fig. S6†. It is noted that the thickness of the electrode after initial lithiation is even reduced compared with its original one, from *ca*. 24 μm for the original one (Fig. S6a†) to *ca*. 15 μm after the initial lithiation (Fig. S6b†). As seen from Fig. S6a and b† that the active material layer becomes dense after the initial lithiation, which is likely that the particles in the electrode, including the 2D-FC and the electron conductive additives of Ketjen black and Super P, rearranged after the lithiation, caused probably by the flow of the liquid electrolyte. However, the thickness of the active material layer after 10 cycles of lithiation is increased to 19 μm (Fig. S6c†), which tends to be looser than the initially lithiated one, indicating a further volume expansion with the cycling. Nevertheless, the layer is still thinner and less dense than the original one. It is inferred that the volume change of the 2D-FC during lithiation is in a low level. Furthermore, the active material layer is still intactly coated on the surface of the copper foil. In comparison, the thickness of the commercial nano Fe_2O_3 particle electrode is greatly increased from *ca*. 21 μm to *ca*. 30 μm even after the initial lithiation, moreover, the active material layer is greatly damaged, as seem from Fig. S6d and e†. The SEM morphologies of the 2D-FC after 10 cycles at the states of delithitation and lithiation are shown in Fig. S7a and b†, respectively. It is found that the 2D flake structure is mostly preserved in either the state of delithiation and lithiation. The fine particles are mostly the electron conductive additives of Ketjen black and Super P. The thickness of the flakes increases and the mesopores are not observed after 10 cycles, which is supposed due to the surface coating of SEI film. In the lithiation state, the surface of the flakes is rough, which is

supposed due to the uneven distribution of Li_2O and Fe clusters. Therefore, it is further concluded that the ultrathin and mesoporous structure of the Fe_2O_3 flakes plays effective role in the stability of the flakes during lithiation and delithiation.

Conclusions

In summary, novel architectured mesoporous Fe_2O_3 flakes encased within an ultrathin carbon skeleton are synthesized via a facile heating method. The flakes show a high aspect ratio with planar size of 1 – 2 μm and a thickness of several nanometers. The reticulated mesopores accommodate greatly the volume expansion during lithiation and facilitate quite the transportation of the electrolyte. The carbon skeleton not only serves as an electron conductor, but also acts as a flexible framework in supporting the integrity of the flake structure and functions as barriers to prevent the aggregation of the Fe_2O_3. The ultrathin thickness of the flakes endows a short diffusion path for lithium-ion diffusion and provides high resistance to the strain caused by the lithium insertion and extraction. The large planar size of the flakes offers large surface contact between the electrode and the electrolyte. These multi-roles of the unique architecture offer high capacity, superior cycling ability and high rate-capability for the Fe_2O_3@C flakes as anode material for LIBs. An initial reversible capacity of 910 mAh g^{-1} at a discharge/charge current of 0.1 A g^{-1} is obtained, and the capacity shows a gradual increase during cycling. A high capacity of 1080 mAh g^{-1} is obtained after 120 cycles. Such unique Fe_2O_3@C flakes are also hopeful to be interested in other application of nano Fe_2O_3-based materials.

Acknowledgements

We acknowledge the financial supports from the National Natural Science Foundation of PR China (NSFC) for Distinguished Youth Scholars (No. 51025102), NSFC project (No. 51371158), Natural Science Foundation of Zhejiang Province (LY14E010004), Program for University Innovative Research Team of the Ministry of Education of China (IRT13037), Pao Yu-Kong International Fund, Zhejiang University, and EPSRC grant No. EP/K002252/1, UK.

Notes and references

1. M. T. McDowell, S. W. Lee, W. D. Nix and Y. Cui, *Adv. Mater.*, 2013, **25**, 4966–4985.
2. S. O. Kim and A. Manthiram, *J. Mater. Chem. A*, 2015, **3**, 2399–2406.
3. Q. Z. Xiao, Q. Zhang, Y. Fan, X. H. Wang and R. A. Susantyoko, *Energy Environ. Sci.*, 2014, **7**, 2261–2268.
4. P. Poizot, S. Laruelle, S. Grugeon, L. Dupont and J. M. Tarascon, *Nature*, 2000, **407**, 496–499.
5. B. Liu, X. L. Hu, H. H. Xu, W. Luo, Y. Sun and Y. H. Huang, *Sci. Rep.*, 2014, **4**, 4229.
6. J. H. Wang, M. X. Gao, D. S. Wang, X. Li, Y. B. Dou, Y. F. Liu and H. G. Pan, *J.Power Sources*, 2015, **282**, 257–264.
7. G. Q. Zhang and X. W. Lou, *Angew. Chem. Int. Edit.*, 2014, **53**, 9041–9044.
8. P. Roy and S. K. Srivastava, *J. Mater. Chem. A*, 2015, **3**, 2454–2484.
9. F. D. Han, Y. J. Bai, R. Liu, B. Yao, Y. X. Qi, N. Lun and J. X. Zhang, *Adv. Energy Mater.*, 2011, **1**, 798–801.
10. M. X. Gao, X. Chen, H. G. Pan, L. S. Xiang, F. Wu and Y. F. Liu, *Electrochim. Acta*, 2010, **55**, 9067–9074.
11. L. Zhang, H. B. Wu, B. Liu and X. W. Lou, *Energy Environ. Sci.*, 2014, **7**, 1013–1017.
12. Z. Y. Wang, D. Y. Luan, S. Madhavi, C. M. Li and X. W. Lou, *Chem. Commun.*, 2011, **47**, 8061–8063.
13. M. H. Chen, J. L. Liu, D. L. Chao, J. Wang, J. H. Yin, J. Y. Lin, H. J. Fan and Z. X. Shen, *Nano Energy*, 2014, **9**, 364–372.
14. J. Liu and X. W. Liu, *Adv. Mater.*, 2012, **24**, 4097-4111.
15. G. X. Gao, S. Y. Lu, B. T. Dong, Z. C. Zhang, Y. S. Zheng and S. J. Ding, *J. Mater. Chem. A*, 2015, **3**, 4716–4721.
16. J. Kan and Y. Wang, *Sci. Rep.*, 2013, **3**, 3502.
17. J. Qu, Y. X. Yin, Y. Q. Wang, Y. Yan, Y. G. Guo and W. G. Song, *ACS Appl. Mater. Inter.*, 2013, **5**, 3932–3936.
18. G. Gao, Q. Zhang, K. Wang, H. Song, P. Y. Qiu and D. X. Cui, *Nano Energy*, 2013, **2**, 1010–1018.
19. Y. Chen, B. Y. Song, M. Li, L. Lu and J. M. Xue, *Adv. Funct. Mater.*, 2014, **24**, 319–326.
20. X. D. Xu, R. G. Cao, S. Y. Jeong and J. Cho, *Nano Lett.*, 2012, **12**, 4988–4991.
21. L. Zhang, H. B. Wu and X. W. Lou, *Adv. Energy Mater.*, 2014, **4**, 1300958.
22. Y. H. Xu, G. Q. Jian, Y. H. Liu, Y. J. Zhu, M. R. Zachariah and C. S. Wang, *Nano Energy*, 2014, **3**, 26–35.
23. Y. Kim, Y. Park, A. Choi, N. S. Choi, J. Kim, J. Lee, J. H. Ryu, S. M. Oh and K. T. Lee, *Adv. Mater.*, 2013, **25**, 3045–3049.
24. X. Z. Wang, J. S. Qiu, J. Y. Qu, Z. Y. Wang and D. S. Su, *RSC Adv.*, 2012, **2**, 4329–4334.
25. J. H. Zhang, B. Yan and F. Zhang, *CrystEngComm*, 2012, **14**, 3451–3455.
26. B. Y. Liu , N. Zhong, C. H. Fan, Y. Zhou, Y. H. Fan, S. Q. Yu, F. H. Zhang, L. H. Dong, Y. S.Yin, Carbon, 2014, **68**, 573 –582..
27. X. Wang, W. Tian, D. Q. Liu, C. Y. Zhi, Y. S. Bando, D. Golberg, *Nano Energy*, 2013, **2**, 257–267.
28. C. Luna, E. D. Barriga-Castro and R. Mendoza-Reséndez, *Acta Mater.*, 2014, **66**, 405–413.
29. S. Yan, Q. S. Wu, *J. Mater. Chem. A,* 2015, **3**, 5982–5990.
30. W. D. Halstead, *J. Appl. Chem.*, 1970, **20**, 129–132.
31. R. Kiyoura and K. Urano, *Ind. Eng. Chem. Proc. Des. Dev.* 1970, **9**, 489–494.
32. T. Fujii, F. M. F. de Groot, G. A. Sawatzky, F. C. Voogt, T. Hibma and K. Okada, *Phys. Rev. B*, 1999, **59**, 3195–3202.
33. T. Yamashita and P. Hayes, *Appl. Surf. Sci.*, 2008, **254**, 2441–2449.
34. H. Cohen, A. Gedanken and Z. Y. Zhong, *J. Phys. Chem. C*, 2008, **112**, 15429–15438.
35. X. Y. Li, Y. Y. Ma, L. Qin, Z. Y. Zhang, Z. Zhang, Y. Z. Zheng and Y. Q. Qu, *J. Mater. Chem. A*, 2015, **3**, 2158–2165.
36. Z. P. Zeng, H. L. Zhao, P. P. Lv, Z. J. Zhang, J. Wang and Q. Xia, *J. Power Sources*, 2015, **274**, 1091–1099.
37. M. F. Hassan, M. M. Rahman, Z. P. Guo, Z. X. Chen and H. K. Liu, *Electrochemi. Acta*, 2010, **55**, 5006–5013.
38. Y. Wu, Y. Wei, J. P. Wang, K. L. Jiang and S. S. Fan, *Nano Lett.*, 2013, **13**, 818–823.
39. J. L. Cheng, B. Wang, C. M. Park, Y. P. Wu, H. Huang and F. D. Nie, *Chem. -Eur. J.*, 2013, **19**, 9866–9874.
40. W. Wei, S. B. Yang, H. X. Zhou, I. Lieberwirth, X. L. Feng and K. Müllen, *Adv. Mater.*, 2013, **25**, 2909–2914.
41. J. X. Zhu, Z. Y. Yin, D. Yang, T. Sun, H. Yu, H. E. Hoster, H. H. Hng, H. Zhang and Q. Y. Yan, *Energy Environ. Sci.*, 2013, **6**, 987–993.
42. Z. Y. Wang, D. Y. Luan, S. Madhavi, Y. Hu and X. W. Lou, *Energy Environ. Sci.*, 2012, **5**, 5252–5256.
43. F. S. Ke, L. Huang, G. Z. Wei, L. J. Xue, J. T. Li, B. Zhang, S. R. Chen, X. Y. Fan and S. G. Sun, *Electrochim. Acta*, 2009, **54**, 5825–5829.
44. J. L. Liu, D. Qian, H. B. Feng, J. H. Li, J. B. Jiang, S. J. Peng and Y. C. Liu, *J. Mater. Chem.* A, 2014, **2**, 11372–11381.
45. Z. Y. Cao and B. Q. Wei, *J. Power Sources*, 2013, **241**, 330–340.
46. B. Jin, A. H. Liu, G. Y. Liu, Z. Z. Yang, X. B. Zhong, X. Z. Ma, M. Yang and H. Y. Wang, *Electrochim. Acta*, 2013, **90**, 426–432.

47. S. Laruelle, S. Grugeon, P. Poizot, M. Dollé, L. Dupont and J. M. Tarascon, *J. Electrochem. Soc.*, 2002, **149**, A627–A634.
48. X. H. Liu, W. P. Si, J. Zhang, X. L. Sun, J. W. Deng, S. Baunack, S. Oswald, Li F. Liu, C. L. Yan, O. G. Schmidt, *Sci. Rep*., 2014, **4**, 7452.
49. J. Lin, A. R. O. Raji, K. W. Nan, Z. W. Peng, Z. Yan, E. L. G. Samuel, D. Natelson and J. M. Tour, *Adv. Funct. Mater.*, 2014, **24**, 2044–2048.
50. P. Wang, M. X. Gao, H. G. Pan, J. L. Zhang, C. Liang, J. H. Wang, P. Zhou and Y. F. Liu, *J. Power Sources*, 2013, **239**, 466–474.
51. D. Su, H. S. Kim, W. S. Kim, G. Wang, *Micro. Meso. Mater*. 2012, **149**, 36–45.
52. Y. Z. Wu, P. N. Zhu, M. V. Reddy, B. V. R. Chowdari and S. Ramakrishna, *ACS Appl. Mater. Interfaces*, 2014, **6**, 1951–1958.
53. S. A. Pervez, D. Kim, U. Farooq, A. Yaqub, J. H. Choi, Y. J. Lee and C. H. Doh, *ACS Appl. Mater. Interfaces*, 2014, **6**, 11219–11224.
54. Q. M. Su, D. Xie, J. Zhang, G. H. Du and B. S. Xu, *Acs Nano*, 2013, **7**, 9115–9121.

Graphical Abstract

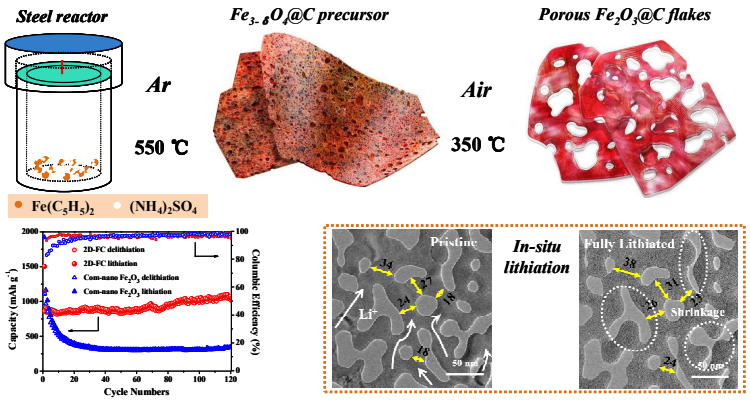

Mesoporous Fe_2O_3 flakes encased within a thin carbon skeleton are fabricated. The unique architecture of the flakes accommodates largely the volume expansion of Fe_2O_3 during lithiation, offering excellent electrochemical properties.